

Prediction of Cellular Structure Mechanical Properties with the Geometry of Triply Periodic Minimal Surfaces (TPMS)

Vladimir Shevchenko, Sergey Balabanov,* Maxim Sychov, and Lyutsiya Karimova

Cite This: *ACS Omega* 2023, 8, 26895–26905

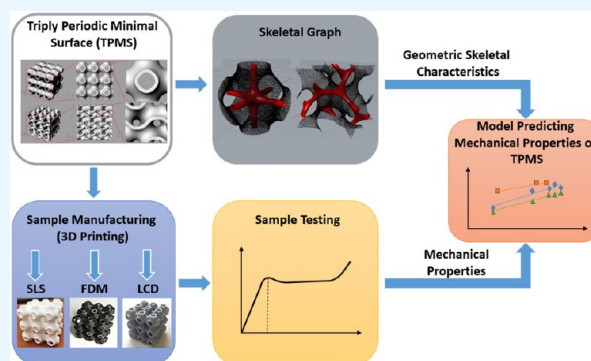
Read Online

ACCESS |

Metrics & More

Article Recommendations

ABSTRACT: The paper investigates the physical and mechanical properties of structures with the geometry of triply periodic minimal surfaces (TPMS). Test samples were made from polyamide using SLS (selective laser sintering) 3D printing technology, from polylactide using FDM (Fused deposition modeling) 3D printing technology, and from a photopolymer based on acrylates using LCD (liquid crystal display) technology; samples were made in the form of a cube with edge size 30 mm. The strength and energy-absorbing properties of TPMS-based cellular samples have been determined. To analyze the features of the geometry of the samples, the skeletal graph method was used. It is shown that this approach makes it possible to predict the physical and mechanical characteristics of products with TPMS geometry.



1. INTRODUCTION

Cellular materials have been actively used in industry for many decades, with the most widespread structures being in the form of hexagonal “honeycombs” that were borrowed from nature. The honeycomb geometry effectively fills the space and has a large surface area inside a certain volume, thanks to this geometric configuration, the products have sufficiently high physical and mechanical characteristics.^{1,2} Materials with the geometry of “honeycomb” are actively used in the aviation and space industry, shipbuilding. Academician V. Ya. Shevchenko showed in their works^{3,4} that due to the unique structure, products with the geometry of triply periodic minimal surfaces (TPMS) have higher mechanical characteristics and significantly exceed classical cellular structures.⁵ It is also significant that the structures used are often found in nature, which makes it possible to count on higher performance characteristics. In particular, the high efficiency of products with TPMS geometries for operation under extreme loads is shown. The use of cellular structures with the geometry of TPMS will allow engineers to significantly expand the possibilities and efficiency of topological optimization in the creation of new equipment. Due to the triply periodic structure, materials with the geometry of TPMS have significantly less anisotropy of mechanical properties, which expands the scope of their application, in particular as energy-absorbing materials.^{6,7}

Thanks to the development of modern technologies, the creation and operation of products with the geometry of TPMS is becoming more and more accessible.^{8,9} To date, the most technologically advanced method of obtaining products with such a complex geometric structure is the 3D printing

method.^{9–12} For a reasonable choice of materials with the geometry of the TPMS, it is necessary to be able to predict their characteristics based on the features of the topology. However, to date, there are practically no theoretical approaches to predicting the mechanical properties of such materials. The presented work shows how the geometric characteristics of the TPMS affect the mechanical properties.^{13,14} In the work,¹⁵ the influence of skeletal geometric parameters on the mechanical characteristics of cellular materials with the geometry of TPMS was evaluated and a new approach was proposed for comparative analysis and prediction of the properties of materials with the geometry of TPMS. This approach is based on the evaluation of the influence of geometry on the mechanical properties of materials. In this paper, this approach is extended to a higher number of topologies and materials.

2. MATERIALS AND METHODS

2.1. Creation 3D Models. Physical and mechanical properties of products whose topologies are based on TPMS were experimentally investigated. At the first stage of the work, 3D models of samples with the geometry of various TPMS instruments were created: Schwartz Primitive (Figure 1a),

Received: March 10, 2023

Accepted: July 4, 2023

Published: July 19, 2023



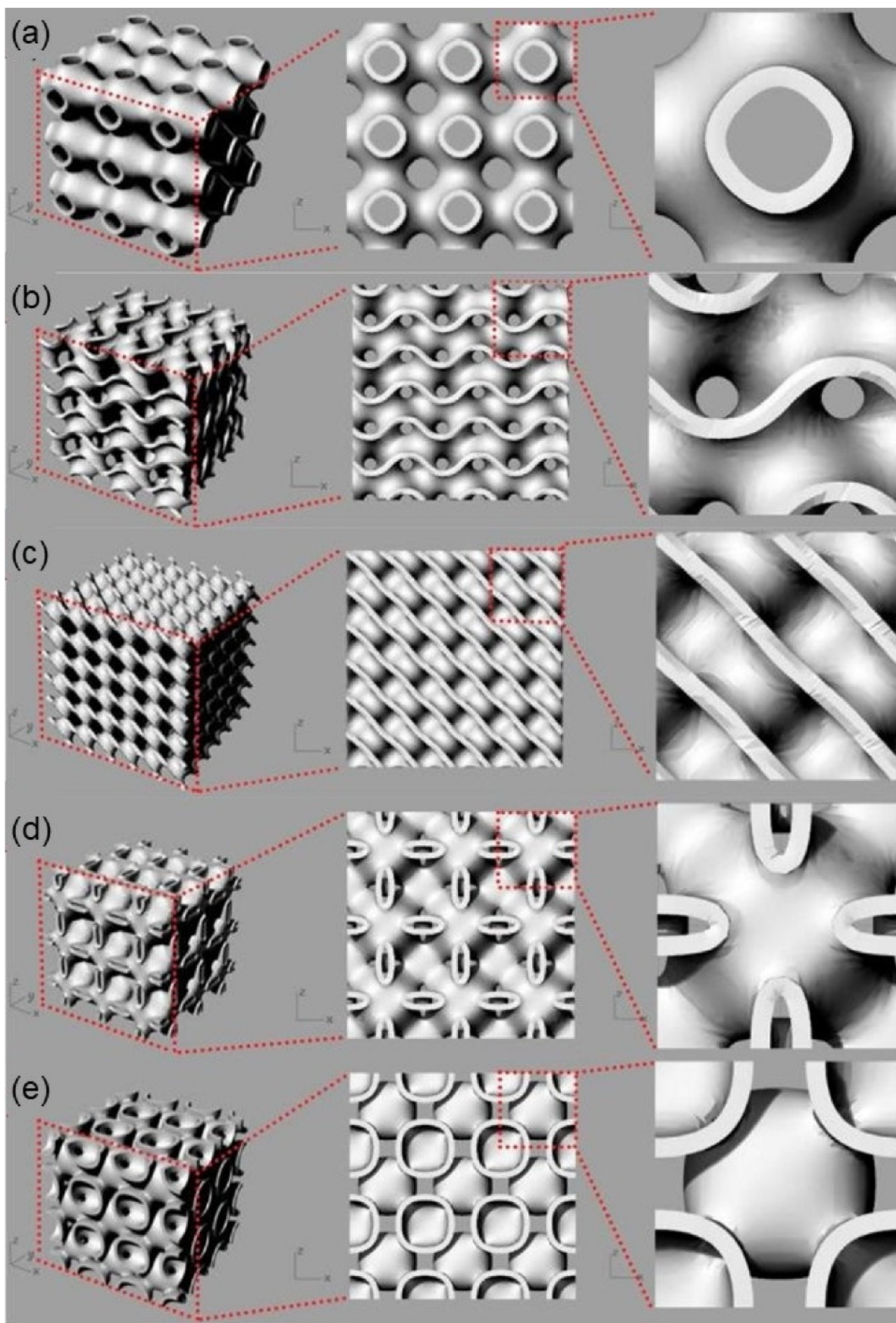


Figure 1. (a) 3D model of the sample with the geometry of the Schwartz primitive. (b) Gyroid. (c) Diamond. (d) Neovius. (e) I-WP.

Gyroid (Figure 1b), Diamond (Figure 1c), Neovius (Figure 1d), and I-WP (Figure 1e).

The forming surface of 3D models of samples is described by a mathematical equation, unique for each type of TPMS.


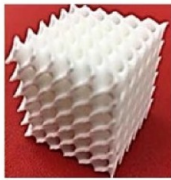













3D printing technology	Schwarz primitive	Diamond	Neovius	I-WP	Gyroid	Material
SLS (selective laser sintering)						Polyamide-12
FDM (Fused deposition modeling)						Poly lactide
LCD (liquid crystal display)						Photopolymer

Figure 2. Samples made using 3D printing.

- P-surface (Schwarz Primitive):

$$\cos(x) + \cos(y) + \cos(z) = t \quad (1)$$

- D-surface (diamond):

$$\begin{aligned} \sin(x)\sin(y)\sin(z) + \sin(x)\cos(y)\cos(z) \\ + \cos(x)\sin(y)\cos(z) + \cos(x)\cos(y)\cos(z) \\ = t \end{aligned} \quad (2)$$

- N-surface (Neovius):

$$\begin{aligned} 3(\cos(x) + \cos(y) + \cos(z)) \\ + 4(\cos(x)\cos(y)\cos(z)) \\ = t \end{aligned} \quad (3)$$

- I-WP surface:

$$\cos(x)\cos(y) + \cos(y)\cos(z) + \cos(z)\cos(x) = t \quad (4)$$

- G-surface (gyroid):

$$\cos(x)\sin(y) + \cos(y)\sin(z) + \cos(z)\sin(x) = t \quad (5)$$

where t is a parameter of the unit cell size.

3D models have been created by parametric modeling methods in the Rhinoceros 6 CAD Software with the Grasshopper plugin and stored in STL format; this format is compatible with 3D printers. Errors in the geometry of the model were corrected with the Autodesk Netfabb Software.

The prototypes are macroporous cubes consisting of two intersecting phases—polymer and air. In the samples, the volume of voids (air phase) is 2–4 times higher than the volume occupied by the polymer solid phase. The proportion of the space filling factor (φ) varies from 0.182 to 0.33. The samples consist of elements continuously repeating in space with the

smallest possible area, which combine surfaces with positive and negative curvature.¹⁶

2.2. 3D Print. In accordance with the created 3D models, 3 series of samples were fabricated. Samples of energy-absorbing structures were made by 3D printing using FDM (fused deposition modeling), SLS (selective laser sintering), and LCD (liquid crystal display) technologies (Figure 2).

The samples were made in the form of a cube with edge size 30 mm and consisted of 27 elementary cells ($3 \times 3 \times 3$ cell). The wall thickness of the samples is 0.8 mm.

2.2.1. Series (SLS). For the final preparation of models and the formation of a control program (g-code) for SLS printing, the EOS Parameter Editor was used. The samples were obtained by selective laser sintering (SLS) on an EOS 3D printer (FORMIGA P110 model). SLS 3D printing technology is based on sequential sintering of powder material layers by using high-power lasers. Printing conditions: layer height 100 μm , table temperature 169.5 $^{\circ}\text{C}$, camera temperature: 150 $^{\circ}\text{C}$. After printing, the samples were cleaned from the remnants of the unsealed powder by processing in a sandblasting machine. The printing material is polyamide-12 (PA2200). Polyamide-12 is a product of polymerization of dodecalactam, and it is a structural crystallizing material with increased elasticity. It is characterized by high cracking resistance, high wear resistance, low moisture absorption, high dimensional stability, and good dielectric properties.¹⁷

2.2.2. Sample Series (FDM). For the final preparation of models and the formation of a control program (g-code) for FDM printing, Cura 3.6.0 software was used. Samples were obtained by layer-by-layer deposition of thermoplastics (FDM technology) on an Anet A6 3D printer. Modeling by layer-by-layer deposition FDM (Fused deposition modeling) is the most common technology of additive manufacturing, based on sequential layer-by-layer deposition of molten filament. Printing conditions: layer thickness: 0.2 mm, extruder temperature 210 $^{\circ}\text{C}$, table temperature 60 $^{\circ}\text{C}$. The printing material is polylactide (PLA), polyester of lactic (2-hydroxypropionic) acid. Due to the presence of an ester group in its composition, polylactide is able

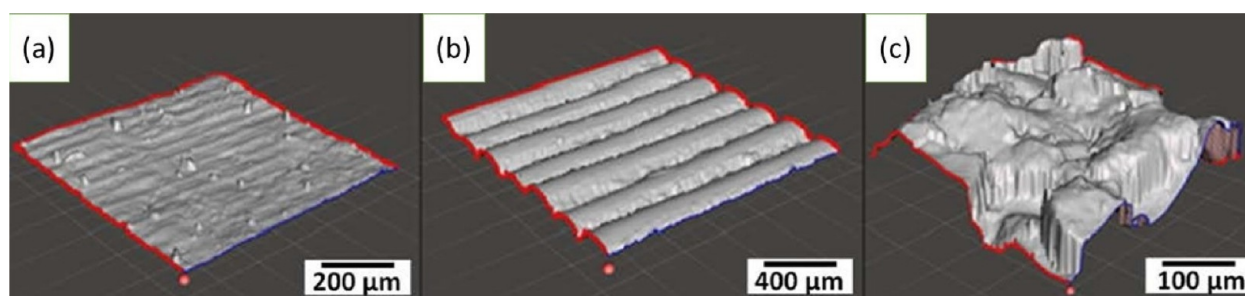


Figure 3. Renderings of 3D models of the surface of samples, samples made using (a) LCD technology, (b) FDM technology, and (c) SLS technology.

to gradually hydrolyze. During the hydrolysis of polylactide, lactic acid is formed; therefore, the use of polylactide-based materials does not damage the biosphere. In addition, it is cheap, nontoxic, and environmentally friendly.¹⁸ This material has great application prospects. The work¹⁹ shows that cellular materials with the TPMS geometry made of PLA have shape memory.

2.2.3. Series of Samples (LCD). For the final preparation of models and the formation of a control program (g-code) for LCD printing, Photon Workshop 2.1.24 software was used. Samples were obtained by layer-by-layer growth of models from liquid photopolymer (LCD technology) on a 3D printer Anycubic Photon S. In the process of 3D printing using LCD (liquid crystal display) technology, ultraviolet radiation from the LCD matrix is selectively directed to a tank with a photopolymer. The screen acts as a mask, showing only the pixels needed to form the current layer. The resin in the tank polymerizes in layers, and the table slowly rises as the part is formed.²⁰ The advantage of LCD 3D printing is high print quality.²¹ Photopolymer compositions based on acrylates are actively used in 3D printing. Polyacrylates are widely used as varnishes, binder components for highly filled plastics processed by injection molding and pressing, adhesives, and sealants. On the basis of epoxyacrylates, high-modulus fiberglass plastics are obtained, characterized by increased chemical resistance.²² Printing conditions: layer thickness: 0.05 mm, layer illumination time: 8 s, and illumination time of the first layers: 70 s. The printing material is a photopolymer resin of the composition: polyurethane acrylate 55%, acrylate monomer 40%, photoinitiator 5%.

To assess the print quality, the surface of the samples was examined by using a confocal laser microscope LEXT OLS5000.

2.3. Mechanical Tests. To study the influence of geometry on mechanical properties, the loading curves of samples during compression were taken in accordance with ISO 604:2002²³ on an electromechanical machine Walter+ bai with a maximum possible load of up to 400 kN, at an air temperature of 25 °C and a loading speed of 5 mm/min. As mentioned earlier, products made by 3D printing have anisotropy of mechanical properties,^{24,25} therefore, strength tests for all samples were carried out in the growth direction (along the Z axis). According to the data obtained, the main physical and mechanical characteristics were determined, the Young's modulus was determined according to Hooke's law:

$$E = \frac{\sigma}{\varepsilon} \quad (6)$$

where σ is stress, ε is deformation

3. RESULTS AND DISCUSSION

To assess the print quality, the surface of the samples was examined using a confocal laser microscope LEXT OLS5000.

Table 1. Properties of Materials for 3D Printing

	Polyamide-12 (PA 2200)	Poly lactide	Photopolymer composition
Compressive strength σ_B (MPa)	57.3 ± 0.7	78.7 ± 1.1	58.3 ± 0.8
Compressive modulus of elasticity E (MPa)	1260 ± 15	1832 ± 20	1287 ± 17
Density ρ (g/cm ³)	1.01	1.21	1.18
Melting point t (°C)	182	175	-
Residual elongation at break δ (%)	12.9 ± 0.3	5.2 ± 0.2	1.86 ± 0.1
Residual relative narrowing of the cross-sectional area at break ψ (%)	9.3 ± 0.2	2.3 ± 0.1	1.7 ± 0.1

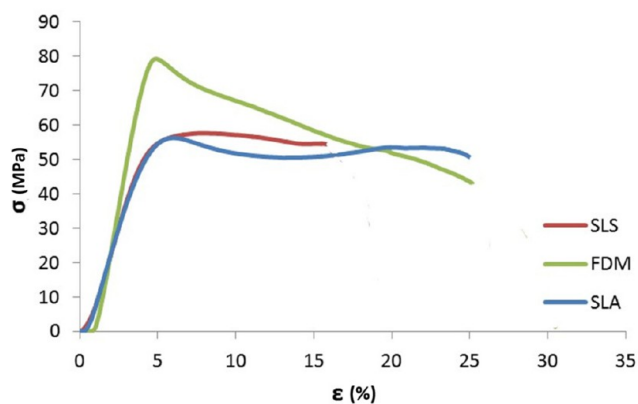


Figure 4. Deformation curves of compression-tested samples manufactured by using various 3D printing technologies.

According to the results of microscopy, no significant defects were found during printing. Renders of 3D models of surfaces are shown in Figure 3. According to the obtained 3D models of the surface, it is possible to evaluate the surface quality (roughness) of the printed samples. The layered structure of the samples is clearly visible on the samples made using FDM and LCD technologies, and the layer height during printing corresponds to the specified 50 and 200 μm for LCD and FDM 3D printing, respectively.²⁶ This structure determines the anisotropy of the physical properties of 3D printed products, including mechanical ones. Samples manufactured using SLS technology do not have pronounced layers, due to which the anisotropy of the properties of products manufactured using SLS technology is less pronounced. But the surface of such products

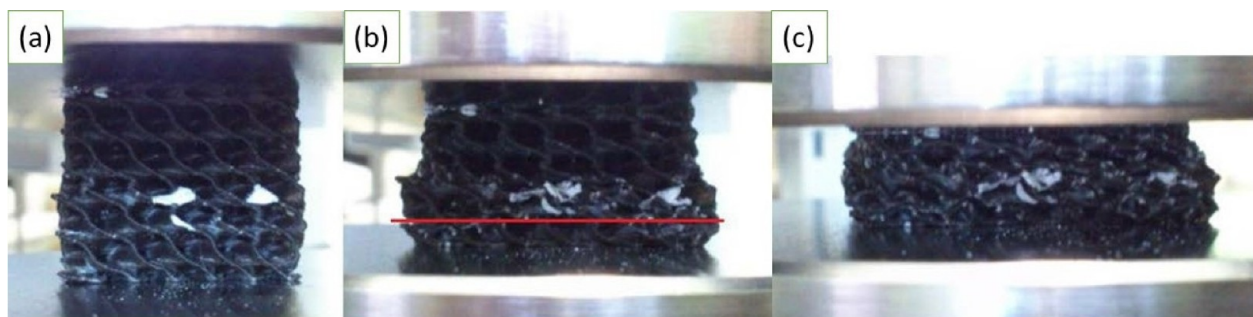


Figure 5. Compression test of a sample with a Diamond topology made using FDM technology: (a) deformation 5%, (b) deformation 30%, (c) deformation 60%.

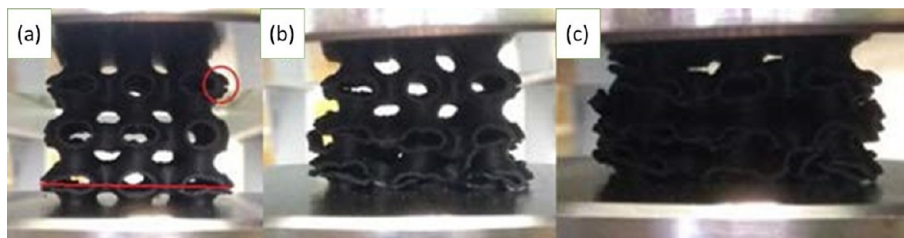


Figure 6. Compression test of a sample with the “Schwartz Primitive” topology manufactured using FDM technology: (a) Deformation 10%, (b) Deformation 25%, and (c) Deformation 40%.

has increased roughness, this is due to the technological feature of this technology, in which a powder with a dispersion of $60\ \mu\text{m}$ is sintered.^{26–28}

Nature of the destruction of materials under external load (plastic or brittle) can be estimated by such characteristics as δ , residual elongation at break, and ψ , residual relative narrowing of the cross-sectional area at break, which are calculated by the following formulas:

$$\delta = \frac{\Delta l_b}{l_0} \quad (7)$$

where Δl_b , elongation of the sample during testing and l_0 is the initial length of the sample

$$\psi = \frac{F_0 - F}{F_0} \quad (8)$$

where F is the area of the minimum cross-section of the neck of the sample after rupture and F_0 is the initial cross-sectional area of the sample.

To determine δ and ψ , the materials used in the work were tested for tensile strength, and the values of δ and ψ for the materials under study are shown in Table 1.

To determine the tensile strength σ_B and the elastic modulus E , the materials were tested for compression; the resulting deformation curves are shown in Figure 4.

Samples from polyamide-12 showed the greatest value, $\delta = 12.9\%$, the lowest value $\delta = 1.86\%$ have samples from photopolymer material, and residual elongation at rupture δ of samples from polylactide is 5.2% . Therefore, we can say that polyamide-12 is the most plastic of the studied materials, and photopolymer composition based on acrylates is the least plastic material, which confirmed the behavior of samples with TPMS geometry during compression testing.

The features of the behavior of polymer materials subjected to forced elastic deformations are usually considered using stress–strain curves. To study the influence of geometric skeletal

characteristics on the mechanical properties of materials with the geometry of TPMS, samples were tested for compressive strength (Figures 5 and 6).

As a result of the tests, the stress–strain curves of the samples were obtained (Figures 7 and 8).

In accordance with the requirements of ISO 604:2002,²³ the first peak on the stress–strain curve was taken as the strength of the samples.

The destruction of samples during compression testing is presented in Figures 5 and 6. It can be seen that the destruction of the studied samples occurs layer-by-layer, which is due to the geometry of the samples. Layer-by-layer collapse during compression can be observed on the stress–strain curves of samples with a large unit cell size; for example, samples with the “Schwartz Primitive” geometry have 3 pronounced peaks on the graphs. And for samples with a small unit cell size, and accordingly with a small layer thickness, the peaks are less pronounced or completely absent, for example, a sample with a Diamond geometry has a smooth stress–strain curve, there are no peaks on it (Figure 7).

The obtained stress–strain curves of samples of the same topology are similar to each other regardless of the method and material of 3D printing.

Samples made using the FDM technology pass into the area of strain-hardening earlier than SLS and LCD samples ($SLS\ \varepsilon_B > LCD\ \varepsilon_B > FDM\ \varepsilon_B$). ε_B is the deformation of the sample at which the ultimate strength is reached (Figure 8). The obtained deformation curves are very close to the dependencies characteristic of classical cellular energy-absorbing structures.²⁹

The deformation curves of the tested samples have three characteristic sections, and the same sections have ideal energy-absorbing structures (Figure 8). Consider the deformation curves of the samples with the geometry “Gyroid”.

To assess the prospects of using products with the TPMS topology as energy absorbers, the characteristics of the samples were analyzed according to.^{29,30} The shock-absorbing characteristics of cellular materials can be calculated on the basis of known

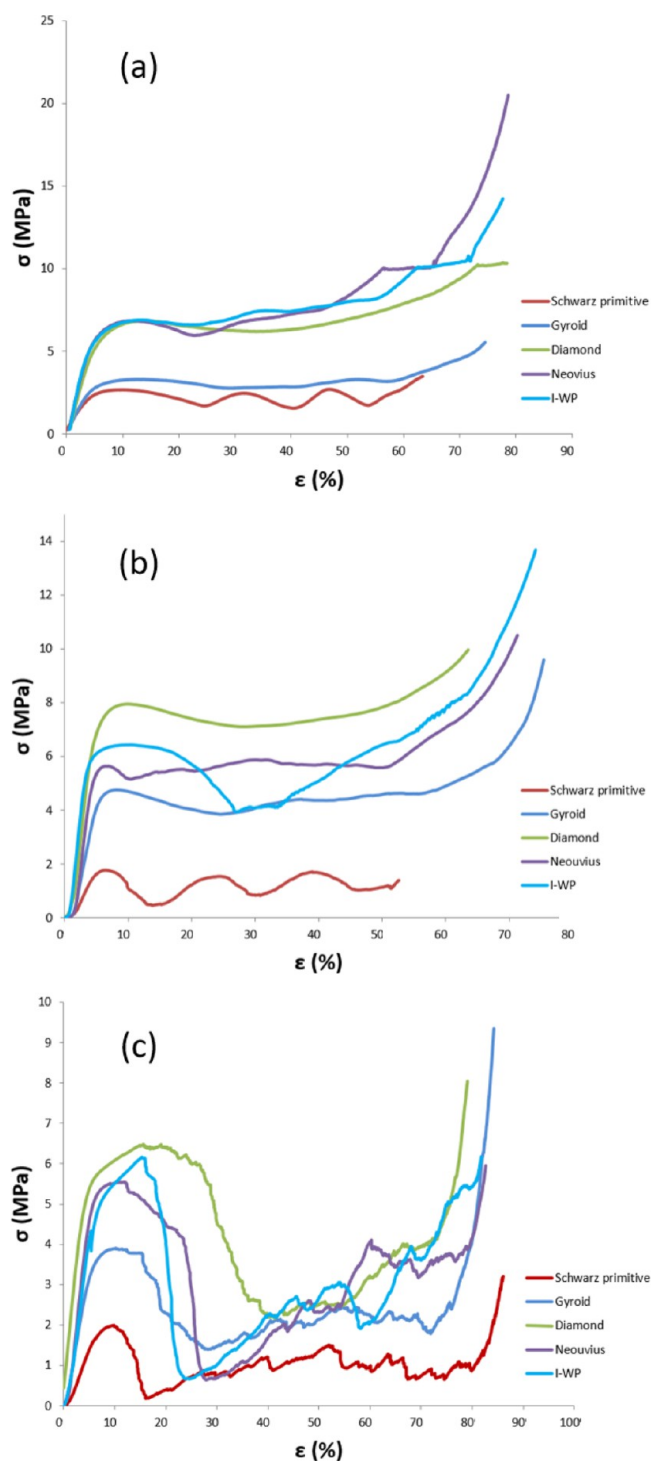


Figure 7. Stress–strain of samples: (a) 1 series, SLS; (b) 2 series, FDM; and (c) 3 series, LCD.

deformation diagrams in the form of shock absorption energy A and effective shock absorption energy E'' . Impact absorption energy (A), Figure 9:

$$A = \int_0^{\varepsilon} \sigma d\varepsilon \quad (9)$$

The effective absorption energy of the sample impact E'' :

$$E'' = \left(\int_0^{\varepsilon} \sigma d\varepsilon \right) / (\sigma_{\max}(\varepsilon)\varepsilon) \quad (10)$$

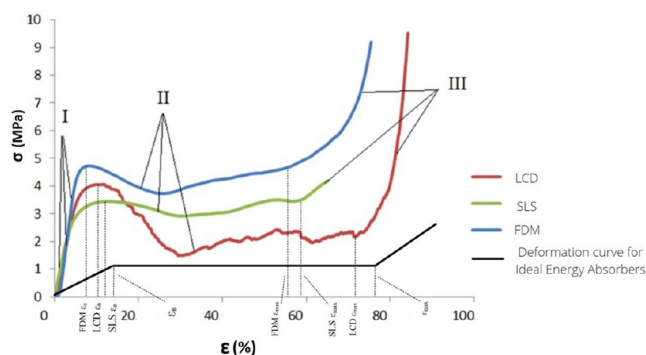


Figure 8. Deformation curves of samples with a “Gyroid” type structure made of different materials.

where $\sigma_{\max}(\varepsilon)$ is the maximum stress reached in the range from 0 to ε .

To assess the energy-absorbing properties of materials, the characteristic A_{30} is energy absorption at 30% deformation ($\varepsilon = 30\%$) (Table 2).

It can be seen that the dependence of the specific energy of shock absorption from deformation in samples made using SLS and FDM technology is almost linear, which indicates the uniformity of energy absorption during deformation of samples under the influence of external forces; the energy-absorbing curves of samples made using LCD technology are nonlinear (Figure 9), this is due to the fact that this material is less plastic and collapses, as a brittle material, unlike polyamide-12 and polylactide. Samples made using LCD technology tend to crack during testing, the samples begin to actively crack and collapse, and when deformed about 20% (Figure 10), while this is not observed in samples made of other materials.

The effective energy of shock absorption E'' is convenient for a comparative assessment of the energy-absorbing properties of cellular structures. It is known that for an ideal energy absorber E'' for an elastic section of the deformation diagram is 0.5, and for a section with a constant stress E'' is 1. To calculate the damping characteristics of cellular structures, their stress–strain curves must be known for large plastic deformations and compaction. This allows us to choose a cellular energy-absorbing structure with rational shock-absorbing properties when developing single-action shock absorbers. According to the graphs shown (Figures 11 and 12), it can be seen that samples made using LCD technology absorb mechanical energy less efficiently. Unlike samples made using FDM and SLS technologies, E'' for LCD samples decreases sharply when deformed by more than 20%, which is due to the peculiarity of the behavior of such samples; when they are compressed, the brittle character prevails destruction (Figure 12).

Based on the results obtained, it can be argued that polyamide-12 and polylactide are more promising materials for the manufacture of energy-absorbing structures than photocured polymers based on acrylates.³¹

The physical and mechanical properties of the tested samples are presented in Tables 3–5.

The difference in the mechanical properties of the tested samples is explained by different geometries. The skeletal graph approach can be used to describe complex geometric objects. Skeletal graphs represent the median axes of the figure. Skeletal graphs for the surfaces of the Schwarz Primitive, Gyroid, I-WP are shown in Figure 13.

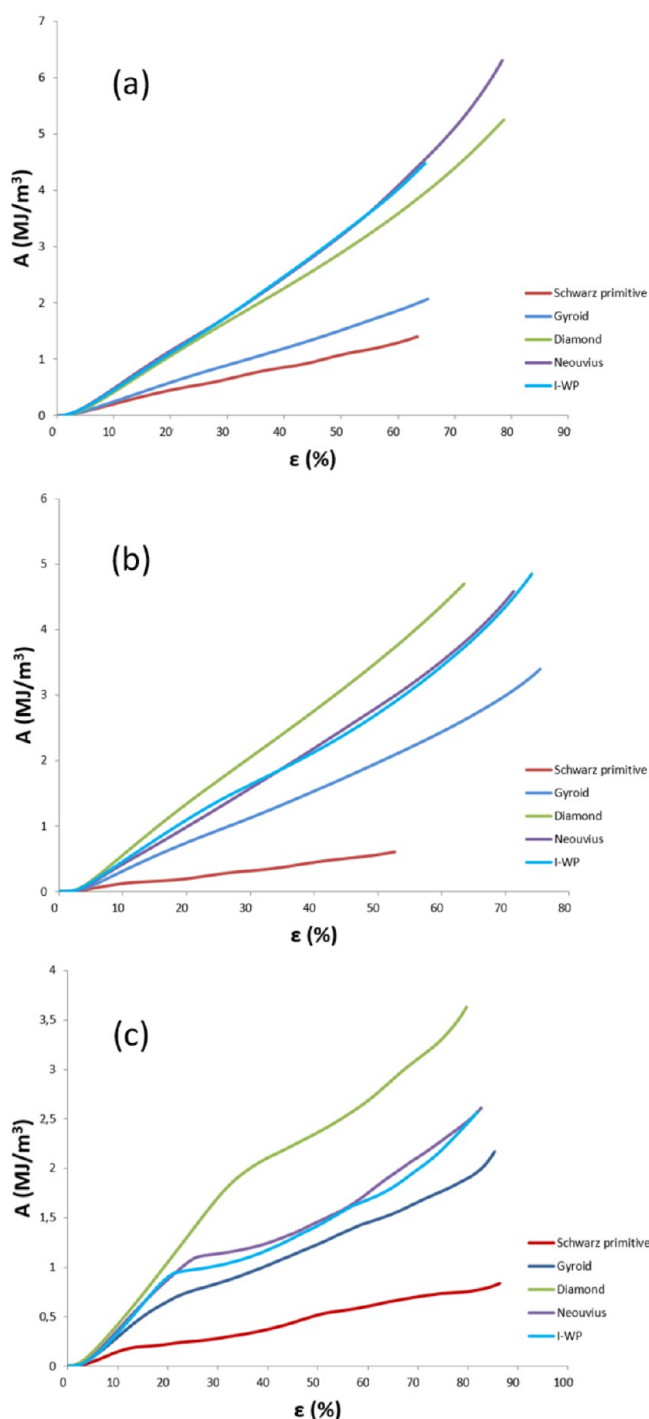


Figure 9. Dependence of energy absorption A_{30} on deformation: (a) 1 series, SLS; (b) 2 series, FDM; and (c) 3 series, LCD.

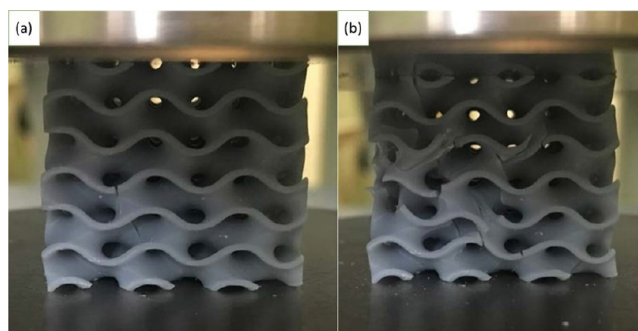


Figure 10. Compression test of a sample with a “Gyroid” topology: (a) 12% deformation and (b) 19% deformation.

The result of an object skeletonization is a set of skeletal geometric parameters. Each type of TPMS has a unique set of skeletal parameters that reflect the geometric features of a particular TPMS. Currently, we are searching for new topologies based on skeletal graphs, in particular, it is proposed to use cellular materials of “Crystallomorphic design”.³² However, an approach is needed for the preliminary screening of promising topologies. Skeletonization can be a good tool for screening new structures of cellular materials. For the studied types of TPMS, skeletonization was carried out according to the work.³³ The results of the skeletonization of the samples are shown in Table 6.

Among the parameters proposed in,³³ correlation with mechanical properties is observed for the following parameters: the total length of arches per unit cell L , the number of arches in unit cell n , the surface area in unit cell S . Then you can enter an effective parameter to

$$K = \varphi L S n \quad (11)$$

Application of the K parameter allows us to accurately predict the physical and mechanical properties of structures with the geometry of TPMS. In accordance with expression,¹⁴ the coefficient K has a high degree of correlation with the specific strength σ of the tested samples, regardless of the material of the samples and the 3D printing technology (Figure 14):

$$\sigma_{\text{spec}} = aK^b \quad (12)$$

where a is the angular coefficient, b is the power coefficient, $0 < b < 0.5$.

Test results of samples with the TPMS topology made using the SLS technology from polyamide-12, obtained in ref 34, also correlate with the value of the K parameter, which confirms the effectiveness of this approach (Figure 14). The specific strength characteristics of the materials under study with TPMS are quite high and grow with increasing values of parameter K . It can be seen from Figure 14 that the dependence is nonlinear, and at low values of the parameter K , the increase in specific strength with

Table 2. Ranking of Samples by Energy Absorption at 30% Deformation

SLS		FDM		LCD		
Topology	A_{30} (MJ/m ³)	Topology	A_{30} (MJ/m ³)	Topology	A_{30} (MJ/m ³)	
1	I-WP	1.76 ± 0.04	Diamond	2.04 ± 0.06	Diamond	1.70 ± 0.05
2	Neovius Surface	1.76 ± 0.05	I-WP	1.63 ± 0.06	Neovius Surface	1.14 ± 0.03
3	Schwartz Diamond	1.67 ± 0.04	Neovius Surface	1.58 ± 0.04	I-WP	1.02 ± 0.03
4	Gyroid	0.90 ± 0.02	Gyroid	1.13 ± 0.03	Gyroid	0.84 ± 0.01
5	Schwartz Primitive	0.65 ± 0.01	Schwartz Primitive	0.32 ± 0.02	Schwartz Primitive	0.28 ± 0.01

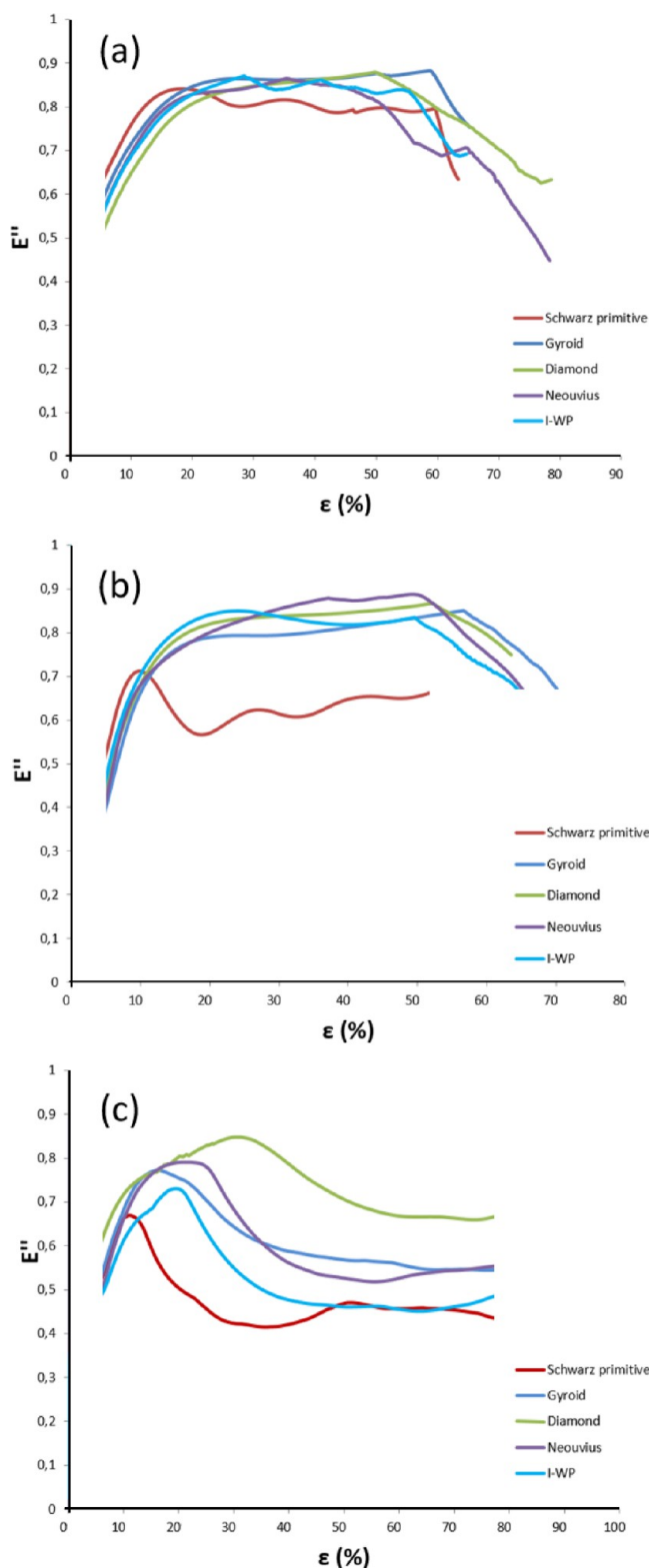


Figure 11. Effective shock absorption energy: (a) 1 series, SLS; (b) 2 series, FDM; (c) 3 series, LCD.

an increase in the value of the parameter K is strong; at large values of the parameter K , saturation is observed.

As a result of the tests, the high-energy-absorbing properties of products with TPMS topology were revealed, which also correlate well with the value of the K parameter (Figure 15). It can be seen from the graph that the higher the value of the

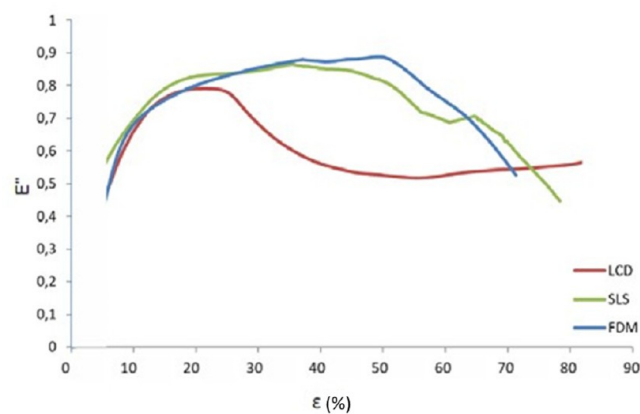


Figure 12. Effective shock absorption energy for samples with “Neovius” geometry.

parameter K , the higher the energy-absorbing properties (A_{30}). The large value of parameter K indicates the geometric “complexity” of the topology, which favorably affects the physical and mechanical properties. Due to the high energy-absorbing properties, products with a TPMS structure are very promising and will find application in various industries.

There is a tendency to increase the level of deformation corresponding to the ultimate strength (ϵ_B) with an increase in the K parameter regardless of the sample manufacturing material and 3D printing technology (Figure 16). As noted earlier, samples made using LCD technology later reach the tensile strength of σ_B , this is due to the fact that there is practically no area of pure sealing-plastic deformation; brittle fracture prevails. Due to the early onset of brittle fracture of the material, the first peak on the curve is wider, and the maximum stress is achieved with greater deformation, unlike SLS and FDM samples ($\epsilon_B > \text{SLS } \epsilon_B > \text{FDM } \epsilon_B$).

The elastic modulus E is one of the main mechanical characteristics of the material, showing its ability to resist the development of longitudinal deformations when testing the sample for axial tension and compression within its elastic operation. The dependence of the elastic modulus on the coefficient K is shown in Figure 17.

An increase in coefficient K indicates an increase in the mechanical properties of the samples, including an increase in elastic modulus E , which means that the ability of the sample to maintain its shape under the influence of external mechanical loads increases. This effect is observed due to an increase in the degree of space filling and the complexity of the geometry, which becomes more complicated with an increase in the value of parameter K .

In the work³⁵ it is shown that classical honeycomb elements have a sufficiently low density and high deformation under load, depending on the properties of the plastic material:

With a density of aluminum honeycombs $\rho = 0.38 \text{ g/cm}^3$, $\sigma_B = 6 \text{ MPa}$, $\sigma_{\text{spec}} = 15.8 \text{ MPa}$.

With a density of aluminum honeycombs $\rho = 0.73 \text{ g/cm}^3$, $\sigma_B = 13 \text{ MPa}$, $\sigma_{\text{spec}} = 17.8 \text{ MPa}$.

Cellular materials studied in this work with the geometry of TPMS have advantages compared with the properties of classical cellular elements. Cellular materials with the geometry of TPMS are more promising as energy absorbers compared to cellular structures since their specific characteristics are higher. It should be noted that, unlike classical honeycomb structures, materials

Table 3. Properties of Structural Elements with TPMS Topology (1 SLS Series)

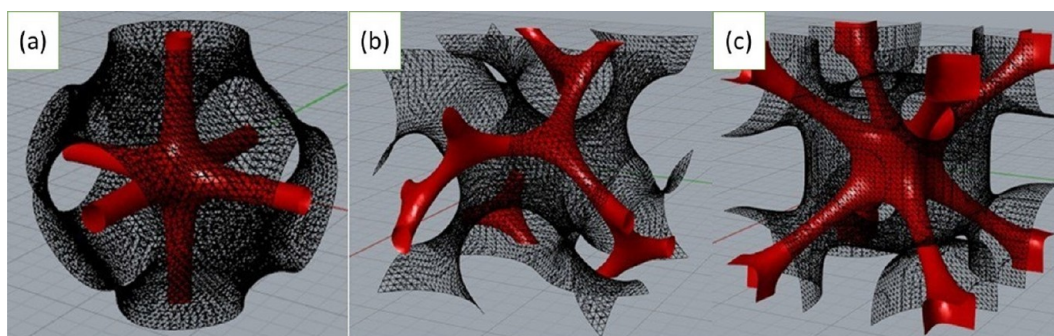
Type of TPMS	Degree of space filling	Strength σ_B (MPa)	Specific strength σ_{spec} ($\frac{\text{MPa cm}^3}{\text{g}}$)	Deformation corresponding $\sigma_B \epsilon_B$ (%)	Young's modulus E (MPa)	ϵ_{max} (%)	Energy absorption at $\epsilon = 30\%A_{30}$ (MJ/m^3)
Schwartz Primitive	0.18	2.67 \pm 0.12	14.6 \pm 0.45	6.9 \pm 0.7	62.8 \pm 3.2	52.2 \pm 1.2	0.65 \pm 0.01
Schwartz Diamond	0.33	5.90 \pm 0.19	20.2 \pm 0.81	10.2 \pm 0.5	105.4 \pm 4.1	71.7 \pm 1.3	1.67 \pm 0.04
Gyroid	0.24	3.10 \pm 0.15	14.0 \pm 0.51	10.4 \pm 0.6	68.9 \pm 3.7	69.7 \pm 1.6	0.90 \pm 0.02
Neovius Surface	0.27	6.25 \pm 0.16	18.0 \pm 0.77	11.7 \pm 0.6	134.2 \pm 3.3	64.3 \pm 1.7	1.76 \pm 0.05
I-WP	0.28	6.00 \pm 0.12	19.6 \pm 0.43	11.2 \pm 0.3	129.4 \pm 3.1	70.0 \pm 1.4	1.76 \pm 0.4

Table 4. Properties of Structural Elements with TPMS Topology (2 FDM Series)

Type of TPMS	Degree of space filling	Strength σ_B (MPa)	Specific strength σ_{spec} ($\frac{\text{MPa cm}^3}{\text{g}}$)	Deformation corresponding $\sigma_B \epsilon_B$ (%)	Young's modulus E (MPa)	ϵ_{max} (%)	Energy absorption at $\epsilon = 30\%A_{30}$ (MJ/m^3)
Schwartz Primitive	0.18	1.72 \pm 0.15	8.6 \pm 0.36	5.1 \pm 0.5	38.3 \pm 2.1	44.8 \pm 1.9	0.317 \pm 0.02
Schwartz Diamond	0.33	8.13 \pm 0.21	24.79 \pm 0.71	9.3 \pm 0.7	134.1 \pm 4.2	51.7 \pm 1.9	2.044 \pm 0.06
Gyroid	0.24	4.73 \pm 0.16	18.25 \pm 0.51	7.7 \pm 0.3	79.2 \pm 2.2	55.1 \pm 2.2	1.127 \pm 0.03
Neovius Surface	0.27	6.16 \pm 0.17	20.52 \pm 0.40	6.8 \pm 0.4	124.4 \pm 3.3	57.6 \pm 1.9	1.579 \pm 0.04
I-WP	0.28	6.49 \pm 90.18	21.48 \pm 0.51	8.7 \pm 0.7	132.2 \pm 4.1	51.4 \pm 1.8	1.629 \pm 0.06

Table 5. Properties of Structural Elements with TPMS Topology (3 LCD Series)

Type of TPMS	Degree of space filling	Strength σ_B (MPa)	Specific strength σ_{spec} ($\frac{\text{MPa cm}^3}{\text{g}}$)	Deformation corresponding $\sigma_B \epsilon_B$ (%)	Young's modulus E (MPa)	ϵ_{max} (%)	Energy absorption at $\epsilon = 30\%A_{30}$ (MJ/m^3)
Schwartz Primitive	0.18	1.86 \pm 0.07	7.31 \pm 0.21	11.1 \pm 0.1	31.3 \pm 0.8	78.8 \pm 0.4	0.28 \pm 0.01
Schwartz Diamond	0.33	6.40 \pm 0.11	15.43 \pm 0.36	16.7 \pm 0.2	113.9 \pm 2.1	68.0 \pm 1.9	1.70 \pm 0.05
Gyroid	0.24	3.88 \pm 0.06	11.56 \pm 0.24	11.1 \pm 0.1	68.4 \pm 0.9	71 \pm 0.3	0.84 \pm 0.01
Neovius Surface	0.27	5.54 \pm 0.05	14.82 \pm 0.19	11.1 \pm 0.1	90.4 \pm 1.7	75.7 \pm 0.9	1.14 \pm 0.03
I-WP	0.28	6.14 \pm 0.09	16.43 \pm 0.32	15.7 \pm 0.2	90.7 \pm 1.9	69.6 \pm 0.8	1.02 \pm 0.03

**Figure 13.** Skeletal graph for (a) Schwartz primitive, (b) Gyroid, and (c) I-WP.

with the geometry of TPMS have significantly less anisotropy of properties.

CONCLUSIONS

- The strength and energy-absorbing properties of cellular samples with the geometry of TPMS are determined. According to the test results, the sample having the structure of TPMS diamond has the greatest strength, the specific strength was: 25 $\text{MPa cm}^3 \text{g}^{-1}$ for polylactide, 20 $\text{MPa cm}^3 \text{g}^{-1}$ for polyamide, 15 $\text{MPa cm}^3 \text{g}^{-1}$ for photopolymer material. The high ability of samples with
- the TPMS geometry to resist deformation under the influence of compressive load was noted, samples made of polylactide using FDM technology have the largest Young's modulus E , and the largest Young's modulus recorded during tests is 134 MPa for the Diamond topology.
- All tested samples demonstrated high energy-absorbing characteristics, but the greatest energy absorption at 30% deformation is possessed by I-WP and Neovius, 1.76 MJ/m^3 for polyamide, and for polylactide and photopolymer material based on polyacrylates, the best topology is Diamond, energy absorption at 30% deformation is 2.04

Table 6. Skeletal Geometric Parameters of TPMS

	Gyroid	Diamond	Schwartz Primitive	I-WP	Neovius
L , arch length in the unit cell	0.707	0.866	2.000	0.707	1.414
D , number of arches in the unit cell	12	16	3	8	12
L , total length of arches per unit cell	8.48	13.86	6.00	13.86	16.97
n , number of arches found in the nodes of the unit cell	3.0	4.0	6.0	4.0	6.4
U , number of nodes in the unit cell	8.0	8.0	1.0	2.0	1.3
S , surface area in the unit cell	12.4	15.50	9.42	14.20	14.13

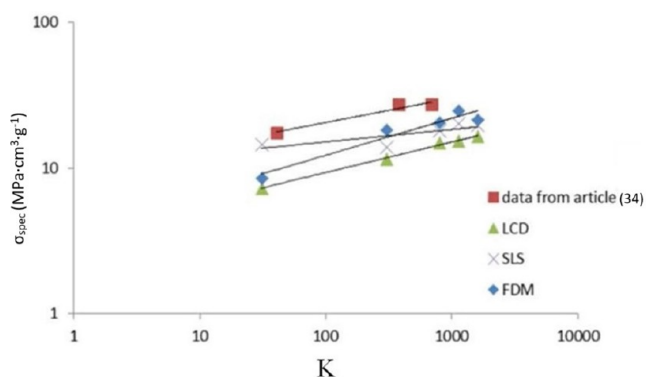
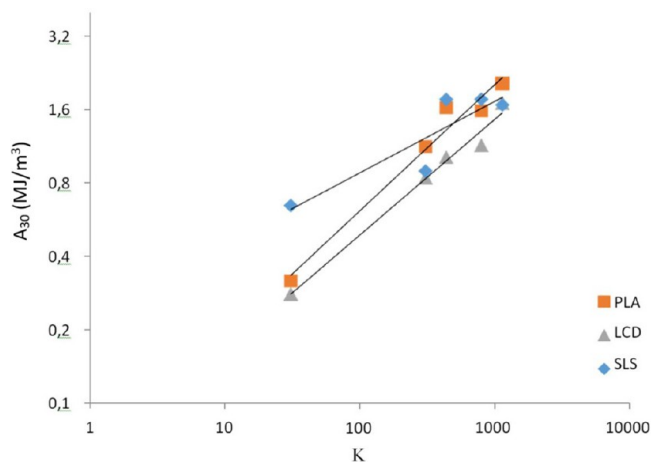
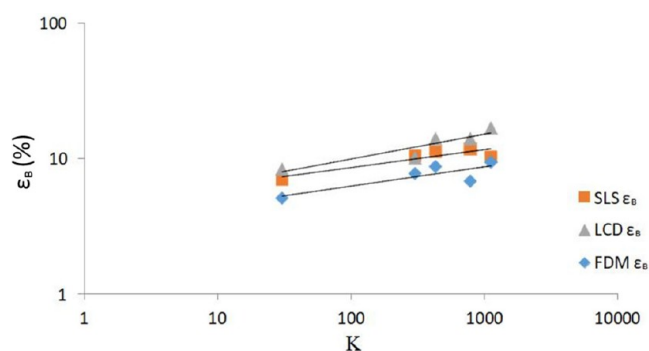
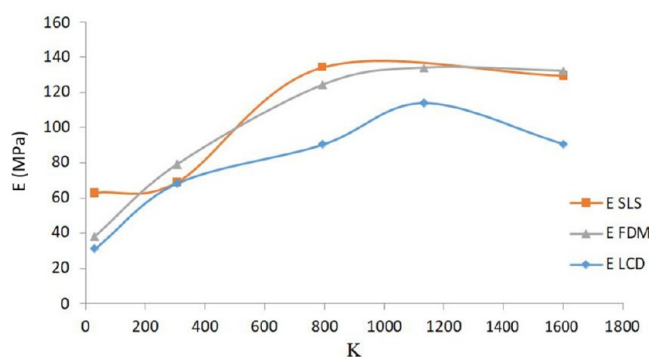


Figure 14. Specific strength of samples.

Figure 15. Dependence of energy absorption A_{30} on the K parameter.

MJ/m^3 for polylactide and $1.70 \text{ MJ}/\text{m}^3$ for photopolymer material.

- Positive correlation has been established between the mechanical characteristics of cellular materials and geometric skeletal characteristics. Thanks to the proposed approach based on the skeletonization of complex geometric objects, it is possible to predict the mechanical characteristics of other cellular structures. Also, topological optimization of the geometry of cellular materials allows for improvement of the geometric characteristics, which in turn will increase the physical and mechanical properties of cellular materials with complex geometry.

Figure 16. Dependence of ϵ_B on the K parameter.Figure 17. Dependence of elastic modulus E on parameter K .

AUTHOR INFORMATION

Corresponding Author

Sergey Balabanov – Institute of Silicate Chemistry, Russian Academy of Sciences, St. Petersburg 199034, Russia;
 orcid.org/0000-0002-2249-350X;
 Email: sergeybalabanov@yahoo.com

Authors

Vladimir Shevchenko – Institute of Silicate Chemistry, Russian Academy of Sciences, St. Petersburg 199034, Russia
 Maxim Sychov – Institute of Silicate Chemistry, Russian Academy of Sciences, St. Petersburg 199034, Russia
 Lyutsiya Karimova – KazGidroMed LLC, Karaganda 100000, Kazakhstan

Complete contact information is available at:

<https://pubs.acs.org/10.1021/acsomega.3c01631>

Notes

The authors declare no competing financial interest.

ACKNOWLEDGMENTS

3D modeling of the samples was supported by the Russian Science Foundation (grant no. 20-73-10171). 3D printing and study of physical and mechanical properties of cellular structures are supported by the State Assignment for the Institute of Silicate Chemistry of the Russian Academy of Sciences (state registration number 0081-2022-0001).

REFERENCES

- Gibson, L. J.; Farris Ashby, M. The Mechanics of Three-Dimensional Cellular Materials. *Proc. R. Soc. London, Ser. A, Math. Phys. Sci.* **1982**, *382* (1782), 43–59.

- (2) Qi, C.; Jiang, F.; Yang, S. Advanced honeycomb designs for improving mechanical properties: A review. *Composites Part B: Engineering* **2021**, *227*, 109393–8368.
- (3) Shevchenko, V. Y.; Sychev, M. M.; Lapshin, A. E.; et al. Ceramic Materials with the Triply Periodic Minimal Surface for Constructions Functioning under Conditions of Extreme Loads. *Glass Phys. Chem.* **2017**, *43*, 605–607.
- (4) Shevchenko, V. Y.; Sychev, M. M.; Lapshin, A. E.; et al. Polymer Structures with the Topology of Triply Periodic Minimal Surfaces. *Glass Phys. Chem.* **2017**, *43*, 608–610.
- (5) Balabanov, S. V.; Makogon, A. I.; Sychev, M. M.; Evstratov, A. A.; Regazzi, A.; Lopez-Cuesta, J. M. 3D Printing and Mechanical Properties of Polyamide Products with Schwarz Primitive Topology. *Technical Physics.* **2020**, *65*, 211–215.
- (6) Xiaojie, F.; Qian, T.; Qixiang, F.; Shuai, M.; Jun, S.; Mengxia, J.; Fuyu, G.; Peng, J. Design, mechanical properties and energy absorption capability of graded-thickness triply periodic minimal surface structures fabricated by selective laser melting. *International Journal of Mechanical Sciences* **2021**, *204*, 0020–7403.
- (7) Xiangyu, Z.; Lan, J.; Xingchen, Y.; Zhipeng, W.; Xiaowei, Li.; Gang, F. Revealing the apparent and local mechanical properties of heterogeneous lattice: a multi-scale study of functionally graded scaffold. *Virtual and Physical Prototyping* **2023**, *18*, e2120406.
- (8) Maskery, I.; Sturm, L.; Aremu, A. O.; Panesar, A.; Williams, C. B.; Tuck, C. J.; Wildman, R. D.; Ashcroft, I. A.; Hague, R. J. M. Insights into the mechanical properties of several triply periodic minimal surface lattice structures made by polymer additive manufacturing. *Polymer* **2018**, *152*, 62–71.
- (9) Han, L.; Che, S. An Overview of Materials with Triply Periodic Minimal Surfaces and Related Geometry: From Biological Structures to Self-Assembled Systems. *Adv. Mater.* **2018**, *30*, 1705708.
- (10) Tian, X.; Zhou, K. 3D printing of cellular materials for advanced electrochemical energy storage and conversion. *Nanoscale* **2020**, *12*, 7416–7432.
- (11) Alomarah, A.; Ruan, D.; Masood, S.; Gao, Z. Compressive properties of a novel additively manufactured 3D auxetic structure. *Smart Materials and Structures.* **2019**, *28*, 085019.
- (12) Qin, Y.; Qi, Q.; Scott, P. J.; Jiang, X. Status, comparison, and future of the representations of additive manufacturing data. *Computer-Aided Design* **2019**, *111*, 44–64.
- (13) Aliaa, M.; Abou, A.; Oraib, A.-K.; Dong-Wook, L.; Reza, R.; Rashid, K.; Abu, A.-R. Mechanical behavior of polymeric selective laser sintered ligament and sheet based lattices of triply periodic minimal surface architectures. *Mater. Des.* **2020**, *196*, 0264–1275.
- (14) Peng, C.; Marzocca, P.; Tran, P. Triply periodic minimal surfaces based honeycomb structures with tuneable mechanical responses. *Virtual and Physical Prototyping* **2023**, *18*, e2125879.
- (15) Sycho, M.; Lebedev, L.; Dyachenko, S. V.; Nefedova, L. A. *Acta Astronautica.* **2018**, *150*, 81–84.
- (16) Lord, E. A.; Mackay, A. L.; Ranganathan, S. *New Geometries for New Materials*; Cambridge University Press, 2006; pp 258.
- (17) Wudy, K.; Drummer, D. Aging effects of polyamide 12 in selective laser sintering: Molecular weight distribution and thermal properties. *Additive Manufacturing* **2019**, *25*, 1–9.
- (18) Ahmed, J.; Varshney, S. K. Polylactides—Chemistry, Properties and Green Packaging Technology: A Review. *Int. J. Food Prop.* **2011**, *14* (1), 37–58.
- (19) Ehrmann, G.; Ehrmann, A. Investigation of the Shape-Memory Properties of 3D Printed PLA Structures with Different Infills. *Polymers (Basel).* **2021**, *13* (1), 164.
- (20) Quan, H.; Zhang, T.; Xu, H.; Luo, S.; Nie, J.; Zhu, X. Photocuring 3D printing technique and its challenges. *Bioactive Materials* **2020**, *5* (1), 110–115.
- (21) Zhao, W.; Wang, Z.; Zhang, J.; Wang, X.; Xu, Y.; Ding, N.; Peng, Z. Vat Photopolymerization 3D Printing of Advanced Soft Sensors and Actuators: From Architecture to Function. *Adv. Mater. Technol.* **2021**, *6*, 2001218.
- (22) Han, H.; Cho, S. Fabrication of Conducting Polyacrylate Resin Solution with Polyaniline Nanofiber and Graphene for Conductive 3D Printing Application. *Polymers* **2018**, *10*, 1003.
- (23) *ISO 604:2002, Plastics - Determination of compressive properties, Multiple*; American National Standards Institute (ANSI), 2007.
- (24) Arsentev, M. Y.; Balabanov, S. V.; Makogon, A. I.; et al. Experimental and Theoretical Studies of the Mechanical Properties of 3D Printed Polyamide Products of the Schwarz Primitive Topology. *Glass Phys. Chem.* **2019**, *45*, 599–602.
- (25) Armstrong, C. D.; Todd, N.; Alsharhan, A. T.; Bigio, D. I.; Sochol, R. D. A 3D Printed Morphing Nozzle to Control Fiber Orientation during Composite Additive Manufacturing. *Adv. Mater. Technol.* **2021**, *6*, 2000829.
- (26) Hartcher-O'Brien, J.; Evers, J.; Tempelman, E. Surface roughness of 3D printed materials: Comparing physical measurements and human perception. *Materials Today Communications* **2019**, *19*, 300–305.
- (27) Dzienniak, D. The Influence of the Material Type and the Placement in the Print Chamber on the Roughness of MJF-Printed 3D Objects. *Machines* **2022**, *10*, 49.
- (28) Kafle, A.; Luis, E.; Silwal, R.; Pan, H. M.; Shrestha, P. L.; Bastola, A. K. 3D/4D Printing of Polymers: Fused Deposition Modelling (FDM), Selective Laser Sintering (SLS), and Stereolithography (SLA). *Polymers* **2021**, *13*, 3101.
- (29) Yuan, S.; Chua, C. K.; Zhou, K. *Adv. Mater. Technol.* **2019**, *4*, 1800419.
- (30) Wei, P.; Liu, L. Influence of density on compressive properties and energy absorption of foamed aluminum alloy. *J. Wuhan Univ. Technol.* **2007**, *22*, 225–228.
- (31) Sankineni, R.; Ravi Kumar, Y. Evaluation of energy absorption capabilities and mechanical properties in FDM printed PLA TPMS structures. *Proceedings of the Institution of Mechanical Engineers, Part C: Journal of Mechanical Engineering Science.* **2022**, *236* (7), 3558–3577.
- (32) Arsent'ev, M. Y.; Balabanov, S. V.; Sychev, M. M.; Dolgin, D. S. Crystalline Design of Cellular Materials. *Glass Phys. Chem.* **2020**, *46*, 657.
- (33) Skeletal Graphs of Triply Periodic Surfaces. <http://www.msri.org/publications/sgp/jim/geom/surface/global/skeletal/index.html>.
- (34) Abueidda, D. W.; Bakir, M.; Abu Al-Rub, R. K.; Bergstrom, J. S.; Sobh, N. A.; Jasiuk, I. Mechanical properties of 3D printed polymeric cellular materials with triply periodic minimal surface architectures. *Materials & Design* **2017**, *122*, 255–267.
- (35) Markov, V. A.; Pusev, V. I.; Selivanov, V. V. *Voprosy Oboronnoj Tekhniki.* **2012**, *7–8*, 54–62 (in Russian).